CHAPTER 2

Laser induced plasma emissions from some planar solid targets

2.1. Introduction

The study of plasma produced by the interaction of a laser with solid matter is an important aspect of many technological applications, such as material processing, pulsed laser deposition (PLD) and chemical trace analysis. In the past decade, considerable effort has been devoted to the solution of basic questions concerning the dynamics of laser induced plasma (LIP) to improve the in situ models of interaction between laser radiation and material and to control technological processes [1,2].

Due to the interaction of high power laser with matter, the vaporization of surface layers leads to the formation of an expanding plasma. During nanosecond laser ablation, high density plasma is heated to high temperatures and is ionized by inverse bremsstrahlung and the photo-ionization processes. The plasma then expands rapidly in the direction perpendicular to the target surface. During the expansion, the main mechanism of transition of bound electrons is driven by inelastic collisions of electrons with heavy particles, while the concentration of charged particles is controlled by the electron impact ionization and the three-body recombination of electrons with ions.

LIP created by a pulsed laser has been investigated with the aim to study possible dynamical mechanisms in different regimes of time and space. The influence of laser energy on the ejection and propagation of different species in the LIP is also being investigated.

2.2. Experimental setup

An Nd: YAG laser (Spectra Physics, Quanta-Ray DCR-11) with an emission wavelength of 1064nm is used as the source of monochromatic radiation for plasma formation inside an evacuated steel chamber. The chamber is pumped down to $2x10^{-5}$

mbar by rotary and diffusion pumps. The laser is operated at a repetition rate of 10Hz, with pulse duration of 10ns. A high resolution monochromator (1m SPEX) coupled with a thermoelectrically cooled PMT and a time resolved detector (gated integrator and boxcar averager, SR 250) interfaced using appropriate software is used to study the time evolution of plasma. The boxcar gate width and monochromator slit width are optimized to maximize the spectral line intensity while maintaining good temporal resolution. For time resolved measurements, each spectrum is recorded at a gate width of 25ns, which is sufficiently short to follow plasma expansion. An aggregate of 10 signal accumulations is collected for averaging.

An optical system consisting of two lenses of equal focal length (f = 150mm) is used to produce a one to one image slice of the plume in a direction perpendicular to its symmetry axis. The targets are placed inside the chamber, on an axle fixed to a motorized rotating system to provide a fresh surface for ablation. An f/4.5 quartz lens (f = 500mm) is used to irradiate the targets with a laser spot of diameter 0.5mm. The detection systems are always triggered using pulses from the pump laser. A digitizing fast oscilloscope (LeCroy 6050A 500MHz) is used to calibrate and control the gate width and time delay after the laser irradiation. A CCD detector (Roper Scientific, NTE/CCD - 1340/100 - EM) coupled to the exit port of a spectrograph (Acton Research, SpectraPro 500i) is used to record the spectral details collected for the time integrated measurements. Studies are made on LIP from pellets of TiO_2, Al_2O_3 and SnO_2, at various energy levels of the pump laser. The powder forms (commercial grade; 99.9 % purity) of the respective oxides are pelletized using a binder, under high pressure and sintered at high temperatures. The pellets used for the experiment are sintered at the best sintering temperature so that the density of the pellet is not different from that of the original material. For comparison purposes, the spectra from the metallic discs of Ti, Al and Sn were recorded with exactly the same geometry and the same laser focusing. For simplicity, the ambient is diffusion vacuum and gas dynamic effects can be safely neglected. Differences appearing in the plasma expansion would be therefore related mainly to the physical phenomena during the laser-matter interaction. Fig 2.1 gives the schematic diagram of experimental arrangements.

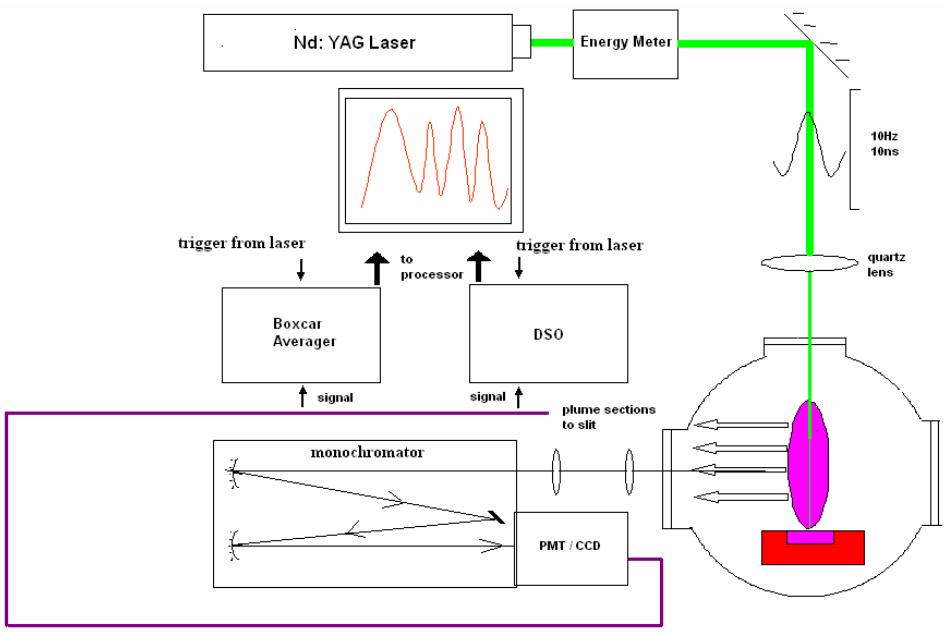

Fig.2.1: Schematic diagram of the experimental setup for optical emission spectroscopy of LIP

2.3.Titanium dioxide and titanium

2.3.1. Plasma emissions and emission profiles

Titanium dioxide is a technologically important material which acts as a photo-sensitizer for photovoltaic cells and as an oxygen sensor. Pulsed laser deposition (PLD) is successfully employed for thin film deposition of materials like TiO_2 and for elemental analysis [3]. TiO_2 films obtained with PLD have numerous optical and thermal applications. Optimization and control of the process demands a better understanding of plasma dynamics. Analysis of optical emissions from plasma is an important diagnostic tool to understand the dynamics of LIP. Moreover, plasma deposited TiO_2 films attract attention due to its high ionic character and comparatively large value of refractive index [4]. For both PLD applications and elemental analysis, it is important to understand the composition and the temporal as well as the spatial evolution of the species in the plasma.

Various experimental techniques can be employed for this purpose. Among them, the most widely used are optical emission spectroscopy (OES), laser induced fluorescence (LIF) and mass spectrometry. Detection of charged particles and laser excitation technique give the best results in the investigation of LIPs far from the target but OES is the simplest way to make the time of flight (TOF) measurements in the high brightness zone of LIP. TOF measurements allow the dynamic aspects of LIP to be studied and give important information on the temporal evolution of species in the plasma plume.

Measurements performed with the experimental setup in Fig. 2.1 yield values that are space-averaged over the whole volume of the considered plasma slice. The laser beam axis is identified as the z-axis and the spectrometer optical axis as the y-axis. In this configuration, the spectrometer entrance slit collects the light emitted by a slice of plasma of thickness Δz along the (x,y) plane. One-dimensional resolution of the ablation plume is achieved by imaging various plasma slices onto the entrance slit of the spectrometer. The experiments carried out at each sampling distance are concerned with the expansion dynamics of the atomic species.

Space resolved OES gives a triple peak distribution exhibited by the TOF profile of Ti I in TiO_2 plasma, above a threshold energy of the pump laser. The evolution of the peaks is studied for various laser irradiances. Their dependence on the distance from the target surface provides some information about their origin. The different peaks are arising from Ti produced by different processes. Particle velocity measurements show a strong collisional expansion.

Optical emissions from excited neutral Ti at 586.6nm [$3d^2.4s^2$ - $3d^2.4s4p$] has been analyzed for time of flight studies. The spectrum exhibits a multiple peak distribution with pump energy increasing beyond 110mJ. At 110mJ of pump energy, a double peak structure (pk1 and pk2 in fig 2.2) is observed. The pk1 is more intense than pk2 till the observation point at 6mm from the target surface. Beyond this, pk2 becomes more intense than pk1 as observed in the figure. A high brightness zone is observed within a distance of 3mm and the intensity is slowly diminished outside the bright zone. This is due to cooling of plasma by recombination processes. In the double peak formation, the delayed peak exists only outside the bright zone. However, at greater energy, the splitting

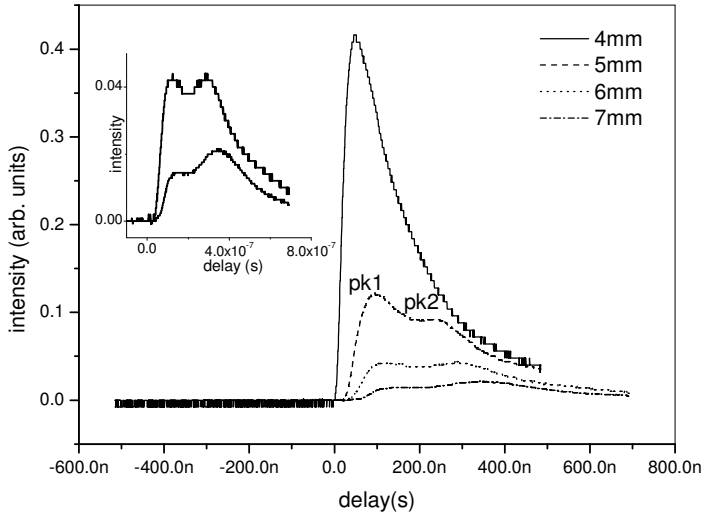

Fig. 2.2: Dual peak distribution of TiI in TiO_2 plasma. Inset shows the plot for 6mm and 7mm. Pump energy is 110mJ.

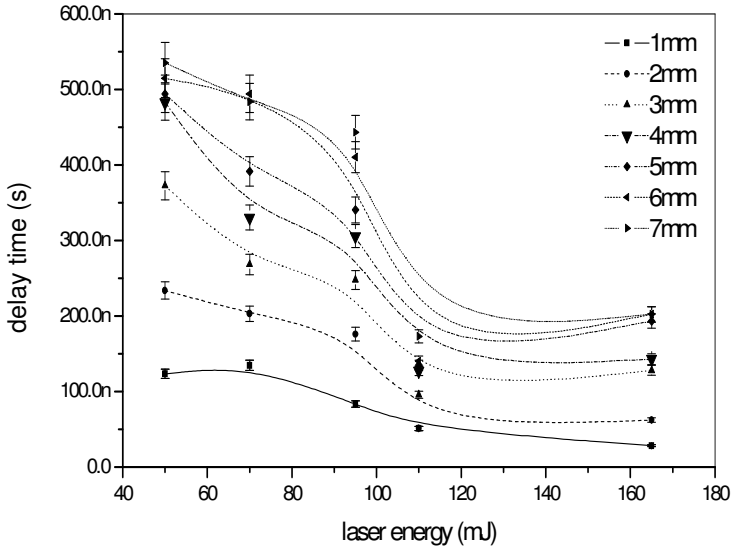

Fig. 2.3: Variation of delay (pk 1) with laser energy at different spatial points from origin of plasma formation. Source - LIP from TiO_2.

is prominent even within the bright zone and a third component (pk3) is observable outside the bright zone. A typical distribution of dual peaks is given in Fig 2.2.

Beyond pump energy around 110mJ, sudden decrease in the delay of pk1 with respect to pump pulse is observed as shown in Fig 2.3. Fig 2.4 depicts the fact that high velocity peak (pk1) initially shows an increase in delay with distance and just beyond the high intensity zone (<3mm), it becomes constant for intermediate distance and then increases with further distances. Delay of pk2 exhibits nonlinear variation with distance, while pk3 shows stronger dependence on delay, with target separation.

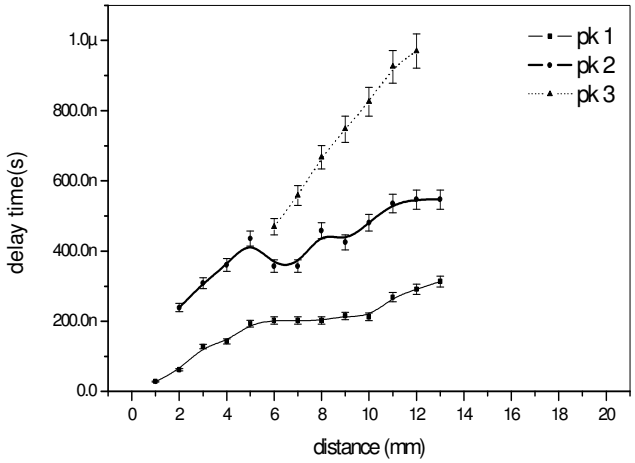

Fig. 2.4: Delay variation of different peaks with distance at laser energy of 165mJ. Source - LIP from TiO_2.

The initial peak structure in the TOF profile of Ti species are assigned to those generated away from the target that is responsible for the higher kinetic energy peak and the most delayed peak to those generated through direct laser ablation or in the vicinity of the target. At intermediate distances, electron impact collision is highly probable and higher excited states are produced. As time evolves, plasma temperature drops so that the excited states undergo collisional recombination with electrons and yields an enhanced spectral emission from Ti [5,6,7]. Such a behaviour is also supported by the fact that emissions of Ti I and Ti II are detected outside the high brightness zone.

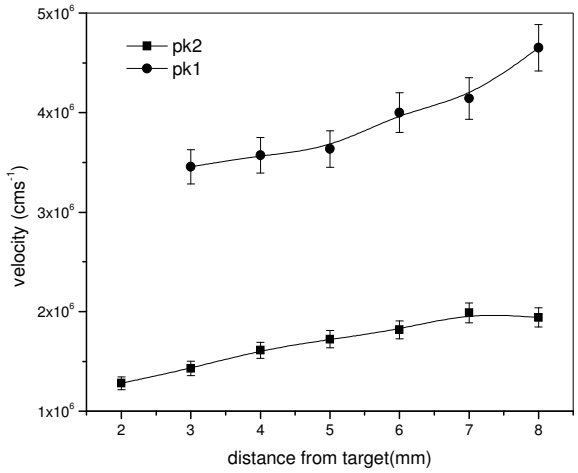

Fig. 2.5: Comparison of pk1 and pk2 velocities in metallic titanium LIP at 250mJ laser energy.

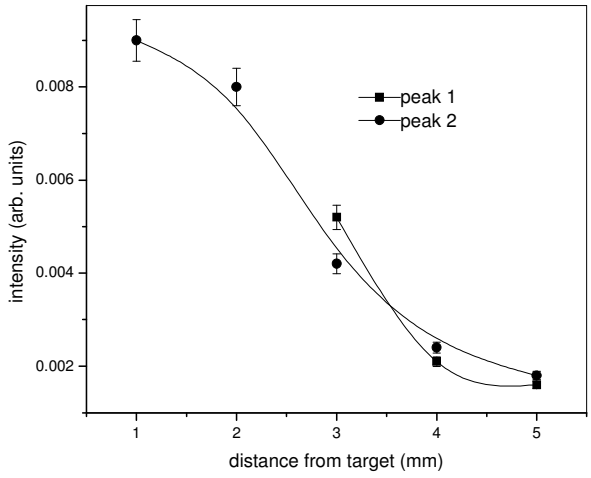

Fig. 2.6: Intensity variation of dual peaks at 100mJ Source – LIP from metallic titanium.

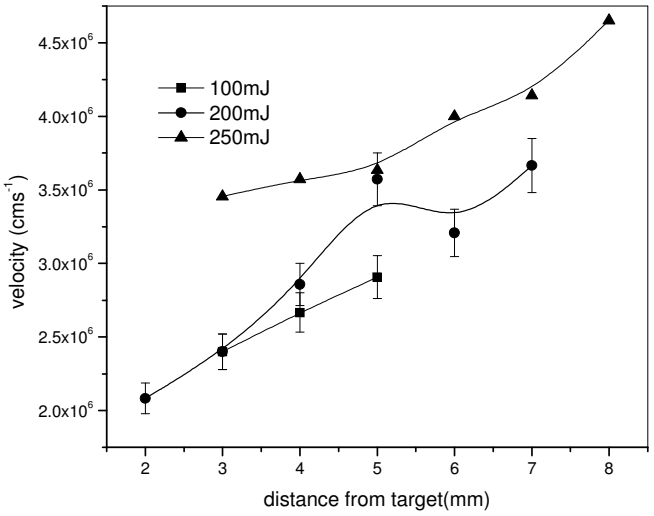

Fig. 2.7:Velocity plot at different laser energies evaluated from pk1. Source – LIP from metallic titanium

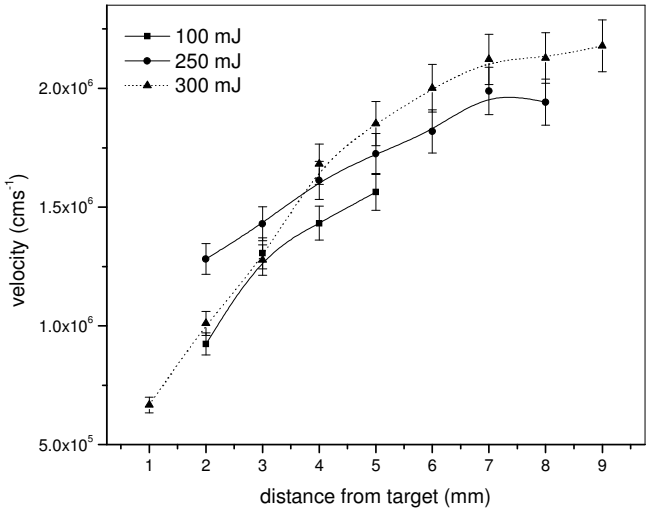

Fig. 2.8: Velocity saturation of pk2 in metallic titanium LIP

The time evolution of LIP species can be used to determine the expansion rate as the distance increases from the target. From the shift of TOF peaks for each distance, the mean velocity of LIP along the propagation axis is obtained. Propagation velocities of different peaks in the optical emission at 6mm from the target are 3 x 10^6 cms^{-1} (pk 1), 1.7 x 10^6 cms^{-1} (pk 2) and 1.3 x 10^6 cms^{-1} (pk3). Velocity of pk1 increases initially and reaches a maximum. This trend is due to initial acceleration of the ablated particles. For

the most delayed peak (pk3), the velocity first decreases and then remains constant. This is attributed to the fact that part of the energy is expended in intra-plume collisions [8].

The TOF spectrum of the same plasma emission (excited neutral Ti at 586.646nm) has been analyzed with pure metallic titanium as the target for plasma production. The presence of twin peaks is clearly evident.

Neutrals present in the LIP of pure metallic targets of Ti also shows Peak 2 from 2mm but peak 1 has been detected only from 3mm onwards. Peak 1 is a high velocity peak (Fig: 2.5) emitted by neutral species produced by recombination of charged ions. At the same time, peak 2 is a delayed one and is produced at the target during the laser pulse. The plasma cools off while expanding in vacuum and the electron temperature at 3 mm has been calculated as approximately 1.2eV by spectroscopic methods. It is also noticed that the peak intensities are falling with increase in distance and decrease in irradiance. Within the spatial region beyond 3mm, peak 2 is more intense than peak 1 as shown in Fig: 2.6. Velocity of peak 1 goes on increasing with distance for different irradiances while for peak 2, velocity attains a steady value at large spatial separations and higher irradiances as is evident from Figs: 2.7 and 2.8.

2.3.2.Time and space evolution of electron density

The interaction of laser beam with solid matter and the consequent plasma generation has been studied for many years. Despite the efforts to exploit the laser - matter interaction for material processing and diagnostic purposes by many workers, some of the aspects still need to be elucidated and clarified. The classical approach in the study of LIP is based on the assumption of local thermodynamic equilibrium (LTE) and optically thin plasma. Using these assumptions, parameters like mass of plasma species, density, temperature and chemical composition of the plasma can be easily determined. In LTE condition, Maxwell - Boltzmann and Saha relations are locally valid. In LIP, where the fast dynamics play a fundamental role, the plasma parameters can change due to the supersonic expansion in shorter time with respect to that necessary for the balancing of elementary processes. The knowledge of deviations from LTE is important to understand the corrections and constraints on the theory to be taken into account for practical applications [9,10]. This point will be discussed further in sections dealing with data analysis.

Optical emission spectroscopy (OES), is based on the intrinsic light emission of LIP and does not need any intrusive systems. The spectral composition at different distances from the target throws light into some of the fundamental properties of LIP, which will help in understanding the main processes that must be taken into account for the analysis of plasma [11]. This represent the behavior of the plasma, along the line normal to the target surface and going through the ablation point on the target.

During the evolution of laser induced plasma, excitation and ionization of the evaporated material occur so that the depositing material is energetically suitable for the film formation. It is then important to determine the thermodynamic parameters of LIP such as electron number density (n_e) and electron temperature (T_e). For this purpose, the emission spectra of LIP have been observed at different distances from the target and varying delay times (t) with respect to the laser pulse. Our interest is mainly concentrated on the initial high density plasma evolution ($t \leq 500$ns). We have chosen spectral lines of Ti I and Ti II for plasma diagnostics. The detection of Stark broadening and displacement of spectral lines allow estimating n_e without considering LTE. The full width at half maximum (FWHM) of a Stark broadened line (in nm), without any ionic contribution is given by the simple relation,

$$\Delta\lambda_{1/2} = 2w\left(\frac{n_e}{10^{16}}\right)\text{nm} \tag{2.1}$$

where, w is the electron impact parameter [12,13].

Stark broadening of the line emission from Ti II transition ($3d^2.4s$-$3d^2.4p$) at 350.5 nm is used to evaluate n_e as a function of space and time. At early times of decay, a highly broadened and shifted line profile is observed, while the width decreases with increasing time and this can be observed from figure 2.9. The value of n_e exhibits rapidly decreasing behaviour (from 1.6 x 10^{16}cm^{-3} at 1mm to 1.2 x 10^{16}cm^{-3}) for distances up to 9mm from the target surface as shown in figure 2.10. Its variation with distance perpendicular to the target (z) approximately follows an inverse dependence on z, which indicates that the initial expansion of the plume is one dimensional and is in agreement with the plume expansion model given by Singh et al [14]. The given n_e distribution fits well to an inverse z dependence of the type $n_e = c + b / (z + a)$ where, $a \cong 5$, $b \cong 4$ and $c \cong 1$. A series of emissions from Ti I are also analyzed for spectral broadening due to Stark effect. Both the emissions from Ti I and Ti II show the same spatial variation. The Stark broadening parameter (w) for Ti I (586.5 nm) is not reported. From the value of n_e obtained through the studies on Ti II line, we can

evaluate w in respect of Ti I line. The parameter w thus obtained has the same order of magnitude reported in similar cases [12].

For the time resolved measurement, a time window of 30 ns is selected to get an optimum resolution. The temporal variations of electron density near the target, at distances of 0.5mm and 1mm from the target are discussed. The observed decay of electron density close to the target and at a spatial separation of 1mm is plotted in Fig.2.11. The temporal variation of n_e in the case of 1mm distance has a fast rise up to a maximum value 5.45 x 10^{16}, which decays to lower values at larger gate delays. The rising part is so fast that it cannot be recorded because of the constraints in the present experimental setup. Here, we observe the high density plasma front, indicated by the intense continuum emission, followed by lower density plasma at later time. For delays greater than 50ns, there is very little change in n_e values. Similar is the case for 0.5mm also. The observation is probably due to recombination processes. The relatively low value at 1mm with respect to that of 0.5mm can be attributed to the plasma propagation [15, 16]. The spatio - temporal evolution of density at an increased energy (200mJ), is as given in Fig.2.12. At the increased laser energy, the density is higher at 1mm and is highly nonlinear function of time delay. A weak dependence of density on time is seen around 3mm. At 4mm distance, there is some kind of modulating dependence of n_e with time delay.

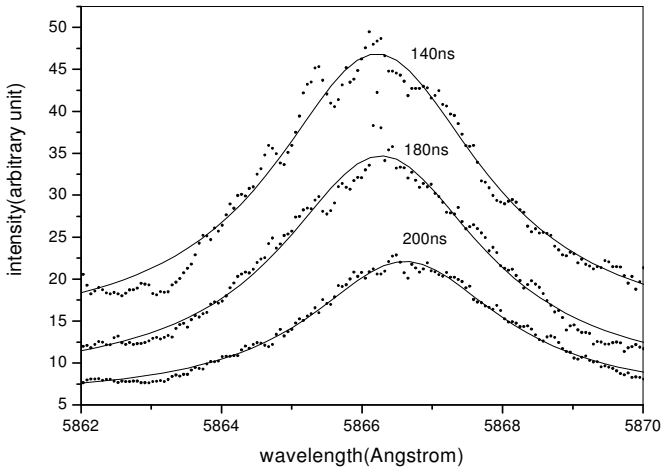

Fig. 2.9: Temporal profile of Ti I (586.5nm) in TiO_2 plasma.

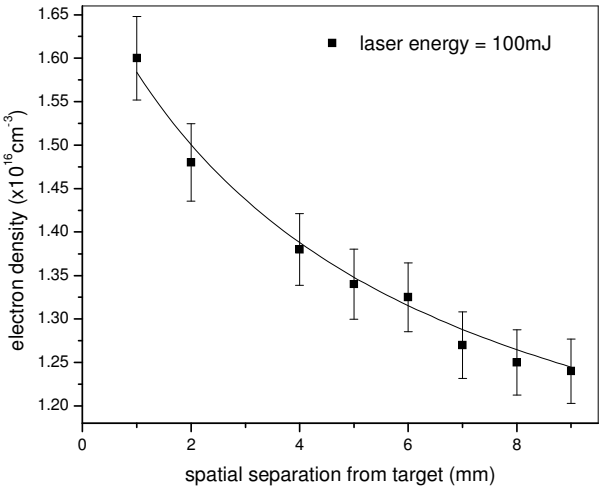

Fig. 2.10: Spatial variation of n_e with 100mJ of laser energy; dotted line shows the theoretical fit based on an inverse z dependence for n_e .Source – LIP from TiO_2.

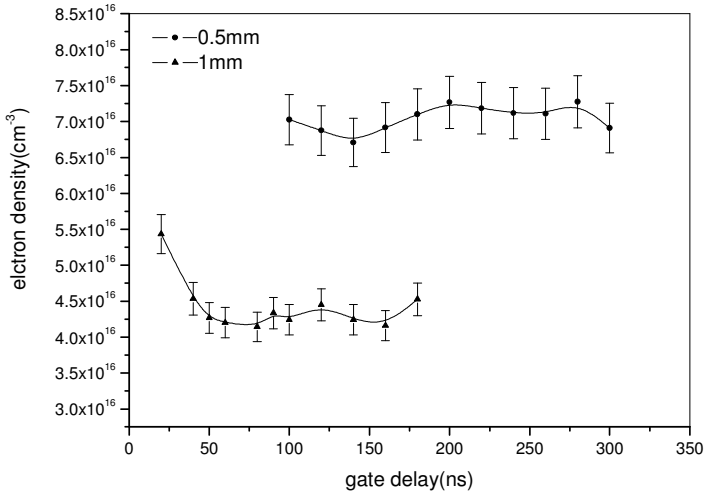

Fig. 2.11:Temporal evolution of n_e from TiO_2 plasma. (Energy of laser beam is 100mJ)

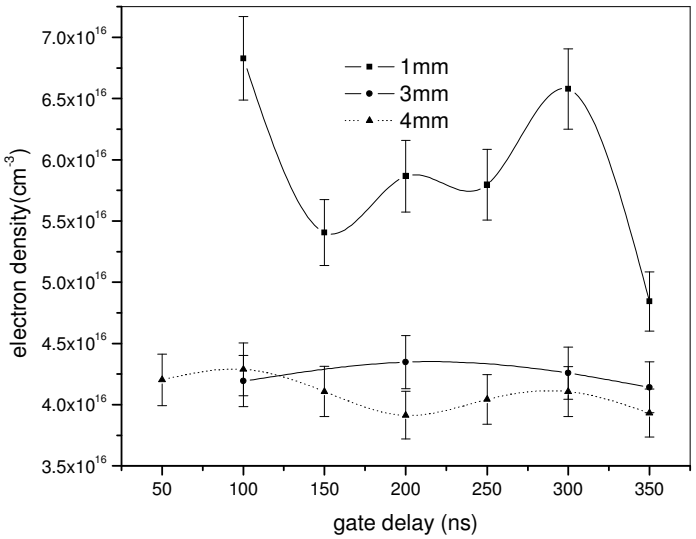

Fig. 2.12: Spatio-temporal electron density evolution in TiO_2 plasma at 200mJ.

The time evolution of line intensities is extracted within a time range extending up to 300ns after the plasma initiation. The typical temporal spectra evolution is shown in figure 2.13. Majority of the emissions are from Ti I and Ti II. The spectral line kinetics of (a) 343.9nm (Ti I), (b) 347.8nm (Ti I), (c) 349.1nm (Ti II), (d) 350.5nm (Ti II), (e) 351.1nm (Ti II), (f) 352nm (Ti II), (g) 353.5nm (Ti II), (h) 357.3nm (Ti II), (i) 358.7nm (Ti II) and (j) 359.6nm (Ti II) are presented. By the analysis of this figure, it is possible to observe the initial spectral continuum, essentially due to collisions of free electrons with heavy particles and radiative recombination of electrons with positive ions. Each fragment of the spectra belongs to a different portion of the LIP temporal distribution.

The emission lines become progressively narrower as a consequence of the change in electron number distribution. The FWHM of a few representative lines, measured at different delay times are shown in Fig.2.13A. It shows that the excitation temperatures must decrease during the time evolution. The maximum intensity is reached after a characteristic time of 90ns, which depends on the observation distance and this represents the most populated section of LIP. As a consequence of the high degree of ionization, for most part of the spectra, the ionic lines are proportionally more intense than those of the atoms, while on the tail of the temporal distribution of LIP intensities, which correspond to the colder part of the plasma, it is possible to observe the progressively disappearing atomic lines.

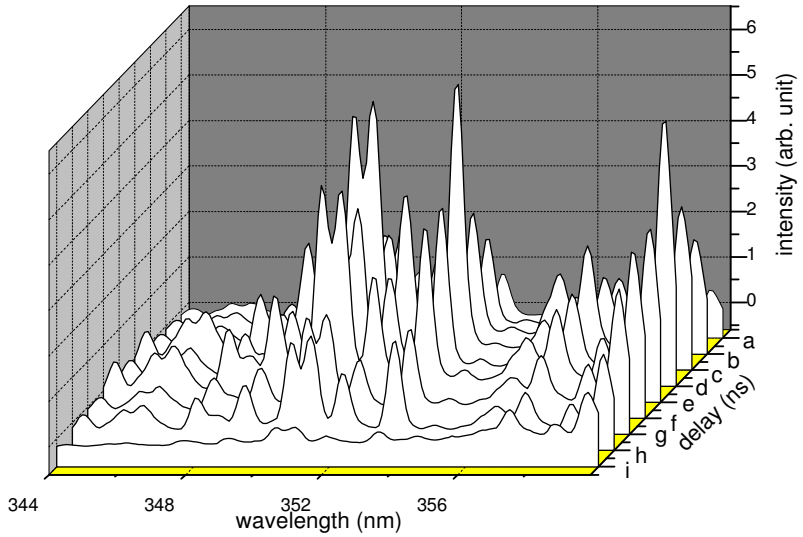

Fig. 2.13:Temporal evolution of a typical Ti spectrum at distance 1mm from the target. (a)20ns (b)50ns (c)60ns (d)90ns (e)100ns (f)120ns (g)140ns (h)160ns(i)180ns.

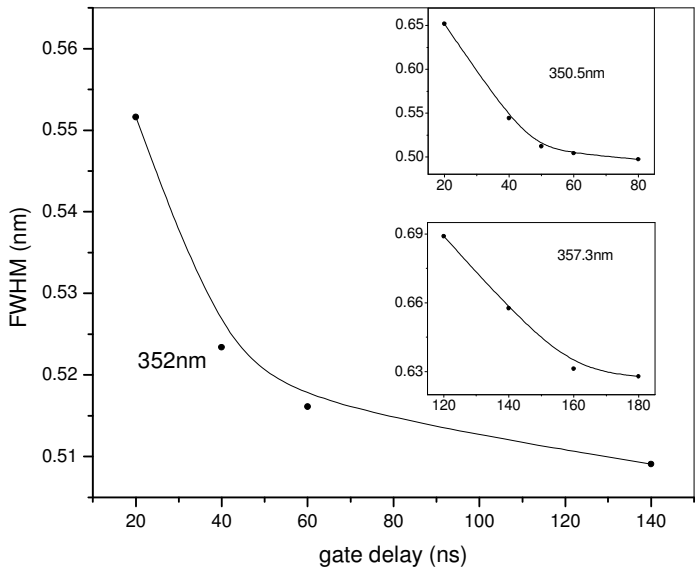

Fig.2.13A: Progressive narrowing of emission line width (352nm), as the plume evolves in time, at 1mm from the target. Inset shows the narrowing feature at 350.5nm and 357.3nm.

The experimental measurement on pure metallic target of titanium (Fig:2.14) shows that density values are lying between definite limits with minimum fluctuations, during 150ns to 350ns except at 1mm separation from the target, where the density is relatively high.

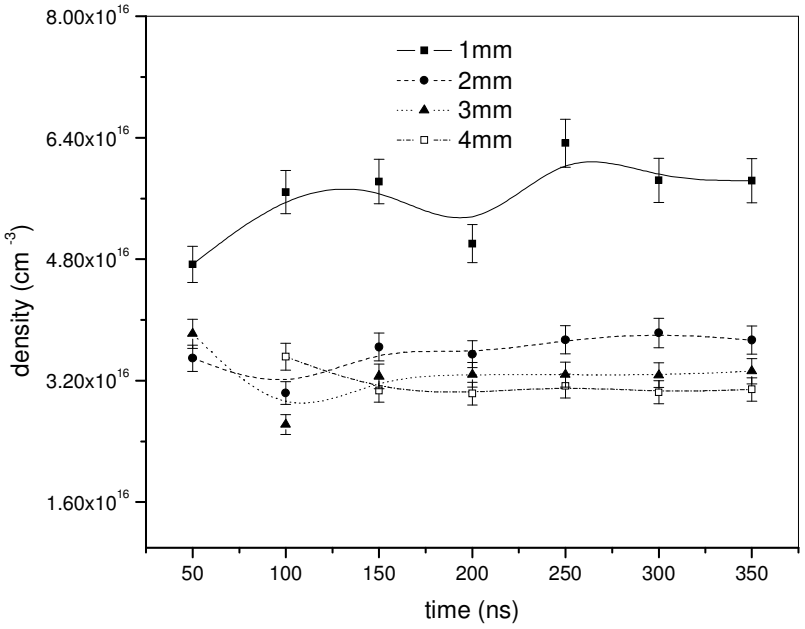

Fig.2.14: Time evolution of electron density of pure metallic target of titanium at 100mJ.

2.3.3. Time and space evolution of plasma temperature: Boltzmann plot method

The electron temperature distribution within time range of upto 350ns is also calculated. While evaluating the electron temperature by this method, it is important to verify that the plasma is not optically thick for the lines used. This was done by checking the ratio of emission intensities at the wavelengths, according to a procedure described by Radziemski et al [17]. The intensities were observed to be in a ratio that is consistent with the ratio of their statistical

weights, which indicates that the plasma was optically thin. The resultant temperature is a population-average temperature as discussed by Boumans [18]. Farther the observation distance from the target (towards the laser beam), colder is the plasma, as depicted in Fig.2.15, due to the expansive dissipation of the plume energy. At a distance of 1mm, the temperature of the tail of the temporal distribution falls down to 1eV from the initial value of 1.2 eV. At 0.5mm from the target, the initial temperature is greater than this. As we go ahead from the target surface, at farther distances, the temperature begins to rise at later times. This can be attributed to the recombination processes which compensate the expansive cooling. With laser energy of 200mJ, the evolved temperature is shown in Fig.2.16. The sudden electron temperature increase at 300ns is due to the laser energy absorption that occurs during the laser – plasma interaction. This can be explained by atom – atom collisions at greater distances from the target [19]. Such an increase can flourish only with tolerable decay rates. But, even at 3mm distance, the recombination rate is not dominant and the increased electron temperature decays faster.

Time integrated measurements are done to evaluate the spatial variation of electron temperature from the target. The measured distribution functions can be represented in good approximation in a Boltzmann form. Assuming a Boltzmann distribution, the plasma temperature can be determined using Boltzmann plot technique using the measurements of spectral intensities (I_{mn}) by the following equation, representing an energy transition from an upper energy state m to a lower state n.

$$\ln\left\{\frac{I_{mn}\lambda_{mn}}{A_{mn}g_m}\right\} = \ln\left\{\frac{N}{2}\right\} - \left\{\frac{E_m}{kT_e}\right\} \tag{2.2}$$

The parameter λ_{mn} is the transition wavelength, A_{mn} is the transition probability, E_m and g_m are the energy and statistical weight of the upper level respectively. The temperature is obtained from the slope of the plot of $\ln\left\{\frac{I_{mn}\lambda_{mn}}{A_{mn}g_m}\right\}$ Vs E_m. We have chosen three transitions of Ti II with well separated upper energy levels in order to determine kT_e. The selected transitions along with their characteristic parameters are listed in table 2.1.

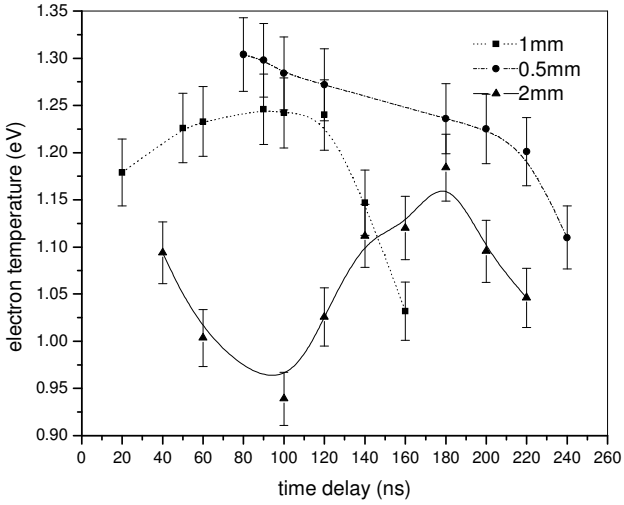

Fig. 2.15: T_e evolution at 100mJ as a function of time. Source: LIP from TiO_2 target.

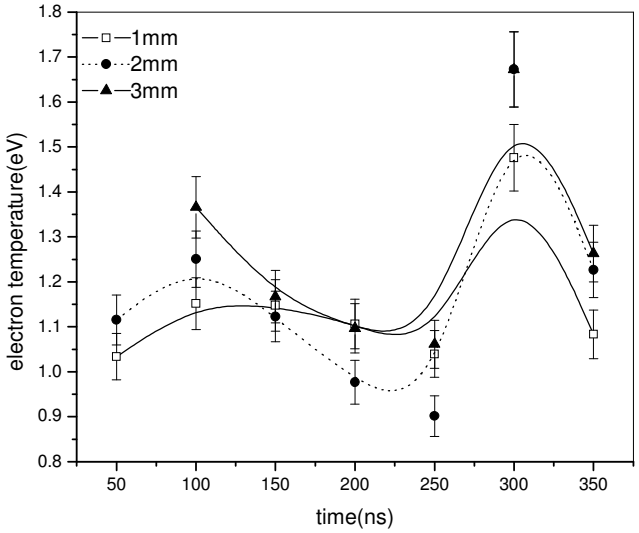

Fig. 2.16: Distribution of electron temperature at a laser energy of 200mJ. Source: LIP from TiO_2 target.

wavelength (nm)	$A(s^{-1})$	g_m	species	E_m (eV)
346.1	$6.27x10^6$	10	Ti II	3.71
348.4	$9.7x10^7$	8	Ti II	7.85
350.5	$6.5x10^5$	10	Ti II	5.42

Table 2.1

The spatial variation of the electron temperature shown in Fig.2.17 is typical with a rapid decay near the target and a slowly varying function of space at larger distances. The lowering of the decay rate of temperature at larger distances is mainly due to the energy gained from three body recombination that compensates the expansive cooling [20]. The calculations are based on the assumption that the emitting species are in collision equilibrium with the electrons and self-absorption for the chosen spectral lines which is due to the absorption by the atoms in the lower level of the transition are neglected.

We confirm the validity of Mc Whirter criterion [21] in the present experiment, which states that the minimum density of LTE should be,

$$n_e \geq 1.4\times10^{14} T_e^{1/2} \left(\Delta E^3\right) \text{ cm}^{-3} \tag{2.3}$$

where T_e and ΔE are in eV. For the transition with the largest energy gap of 3.574 eV, applying the peak plume temperature of 1.67eV to this criterion predicts a lower limit of 8.25 x 10^{15} cm^{-3} for n_e. Our observed n_e values are always greater than this lower bound, implying that LIP from TiO_2 target, under the present experimental conditions validates LTE.

Within the range of laser fluence and temperature studied, excited species of Ti II are prominent in the LIP from TiO_2 target. Spectral lines of oxygen or molecular species are not observed under the present experimental conditions. Majority of the emissions are due to Ti II during the interval upto 180 ns. At a spatial separation of 1mm from the target, the most populated section of LIP emerges after 90ns.

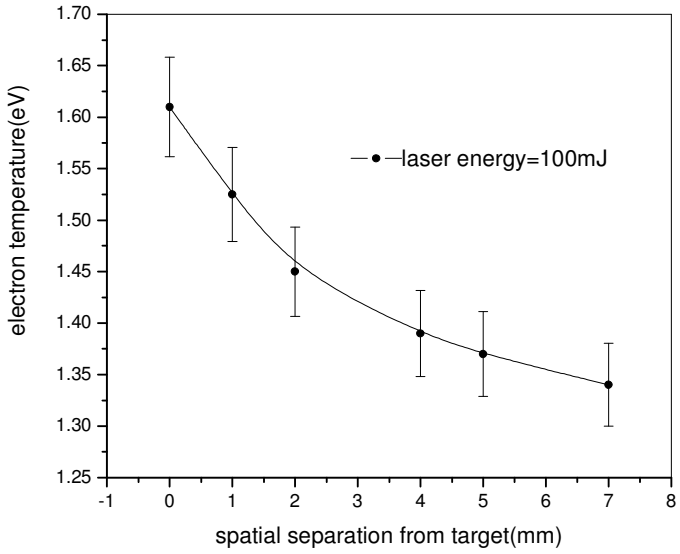

Fig.2.17: T_e distribution in TiO_2 plasma at 100mJ.

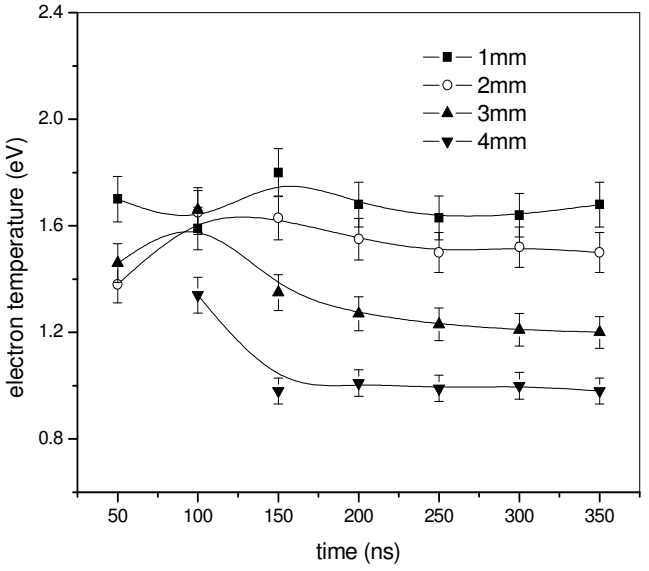

Fig. 2.18: Temporal variation of electron temperature at 100mJ. LIP target is titanium metal

For the plasma produced using pure metallic target of titanium, the electron temperature in the region from 1mm – 4mm lies between 0.8eV and 1.8eV during the

first 350ns. After 150ns, the electron temperature at each spatial point shows steady values under the present experimental conditions (Fig: 2.18).

2.4. Aluminium oxide and aluminium

Plasma ignition threshold of aluminum is approximately 0.3 $GWcm^{-2}$ [22]. But at irradiance above 10 $GWcm^{-2}$, a threshold seems to occur indicating a significant change in plasma dynamics from normal ablation to explosive boiling. The sudden change in the mechanism is responsible for vapor and particle formation above the sample surface and subsequent laser plasma interaction. When the laser energy deposited onto the sample is larger than the value required for reaching the critical temperature, the excess of laser energy is directly coupled with the sample and the amount of ablated material is significantly increased.

2.4.1.Time of flight for plasma species

An ionic line of aluminium has been selected for the temporal measurement of line shapes. This line corresponds to the emission from the first excited state (*Al II*) for the transition 3s.4p $^3P^0_2$ – 3s.4d $^3D_3$. For this emission at 624.3nm, the transition probability value is very high, compared to the nearer transitions. The time of flight spectrum is shown in Fig.2.19.

With aluminium oxide target, the expansion velocity is large at distances very close to the target surface and shows irradiance dependence. But at locations away from the target surface, steady cooling occurs in the plasma (at 6mm, the plasma temperature is calculated as 1.3eV). Due to this cooling, the temperature falls below the ionization energy and three body recombination dominates collisional recombination, in the plume regions at larger distances [23]. But at distances below 5mm, collisions are highly prominent and the high initial kinetic energy values of the species are degraded. Beyond 5mm, the expansion velocity of aluminium ions increases slightly with distance up to 14mm but in a steady manner (Fig.2.20). With metal target, the electron density falls (Fig.2.24) with distance from target and the ionic species show that the plasma is freely expanding (Fig.2.21).

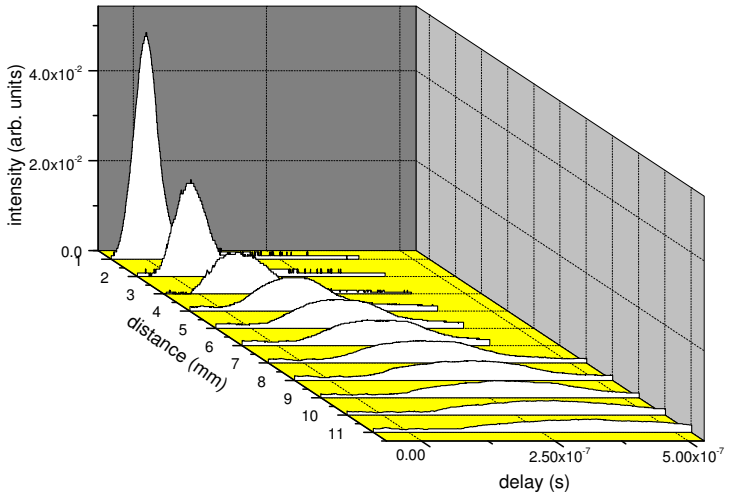

Fig. 2.19: Flight of AlII from 1mm to 11mm in aluminium oxide plasma at 200mJ laser energy

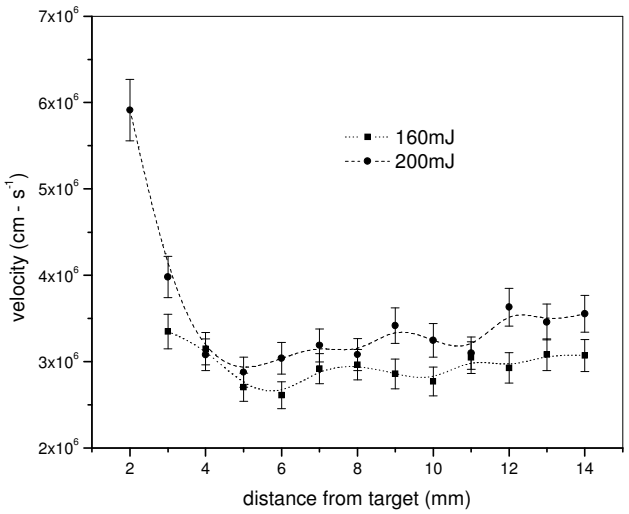

Fig. 2.20: Expansion velocity of aluminium ions in aluminium oxide LIP at different laser energies

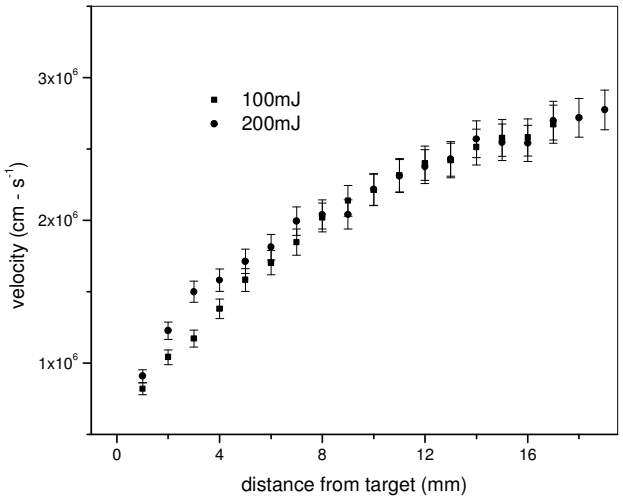

Fig. 2.21: Free expansion of ionic species in LIP of metallic aluminium

The reduced rate of collisions prevents the sudden cooling of plasma as evident from the rapid decrease in emission intensity in the beginning which then becomes very slow (Fig.2.22).

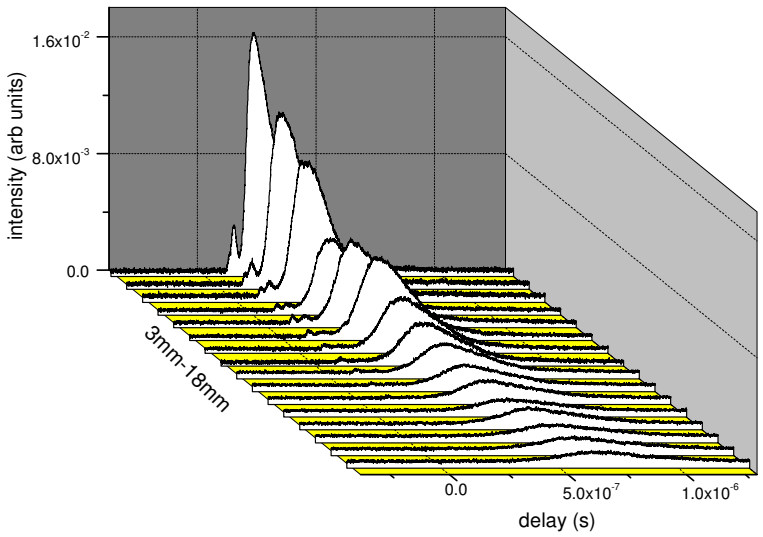

Fig. 2.22: Slow decay of emission intensity at farther plasma slices in aluminium LIP

2.4.2. Development of electron density in space and time

Line broadening and shifting are the result of interaction between emitting species and surrounding electrically charged species (Stark effect), while other possible contributions could be the instrumental broadening, resonance broadening, Doppler and van der Waal's effect [24]. Stark broadening of the line is mainly due to the influence of the free electrons surrounding the emitting particle, that of the surrounding ions being of less importance. The Stark broadening of the neutral aluminium species in the plasma is considered for evaluating the electron density evolution in space and time. All other contributions to the total line width have been neglected in doing this. The line corresponds to the *Al I* emission at 396.2nm, from the transition $3s^2.3p\ ^2P^0_{3/2} - 3s^2.4s\ ^2S_{1/2}$. The spectroscopic data used for the evaluation were retrieved from NIST electronic database [25]. Two sets of measurements are done – density from near field emissions (1mm-6mm) and density from far field (>6mm) emissions. Higher electron density is observed above the oxide surface than the corresponding metallic surface under the most identical situations (Fig. 2.23-2.24).

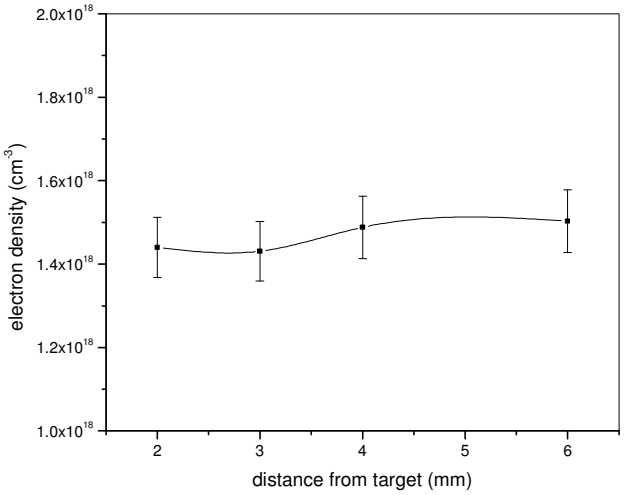

Fig.2.23: Time integrated electron density in the near field of LIP over aluminium oxide target

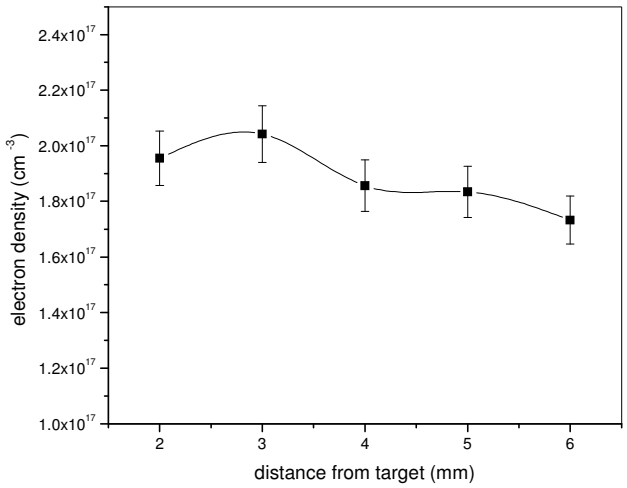

Fig. 2.24: Time integrated electron density. Source – near field emissions from LIP over metallic aluminium target

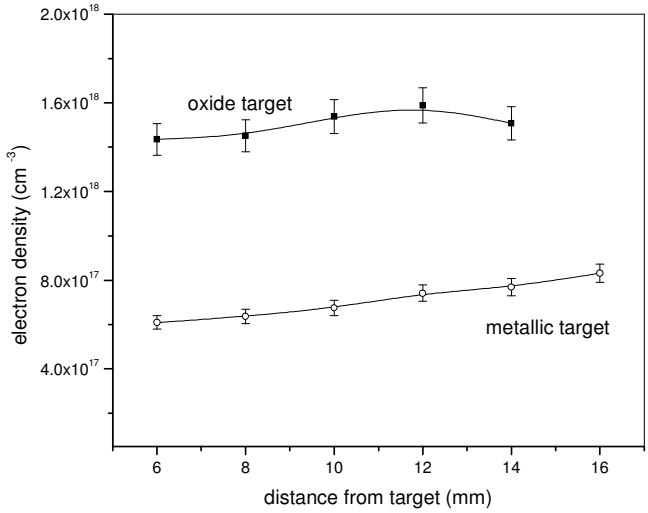

Fig. 2.25: Time integrated electron density in far field region of aluminium LIP

At intermediate distances, the evolved local electron density is preserved without much variation, within the measured time range (Fig.2.26-2.27).

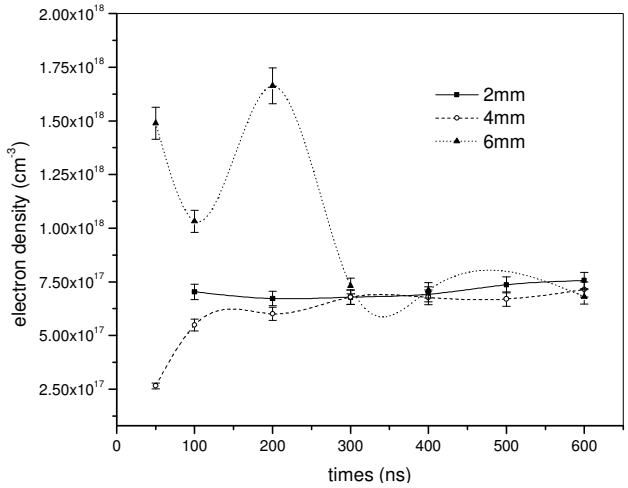

Fig. 2.26:Local electron densities in Aluminium LIP at different times

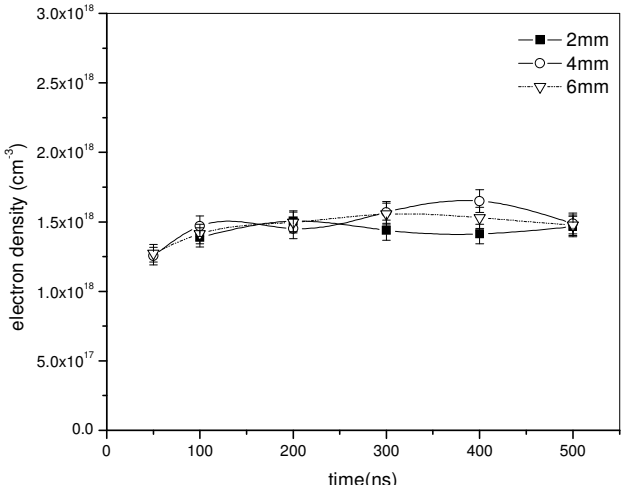

Fig. 2.27: Time dependent variation of local electron densities in the LIP from oxide target of aluminium

In aluminium oxide plasma, the density is lying between $1.4x10^{18}cm^{-3}$ and $1.5x10^{18}\ cm^{-3}$, before 6mm, during its time evolution between 200ns and 500ns. But for the metallic target, the plasma density reaches a high value ($\approx 10^{18}\ cm^{-3}$) between 200ns and 500ns and again falls with distance at 500ns (Fig.2.28-2.29).

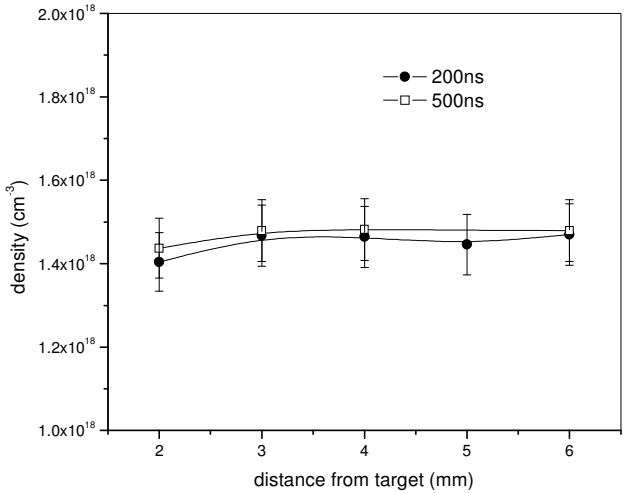

Fig. 2.28: Time resolved variation of spatial electron density. (source – LIP from aluminium oxide target)

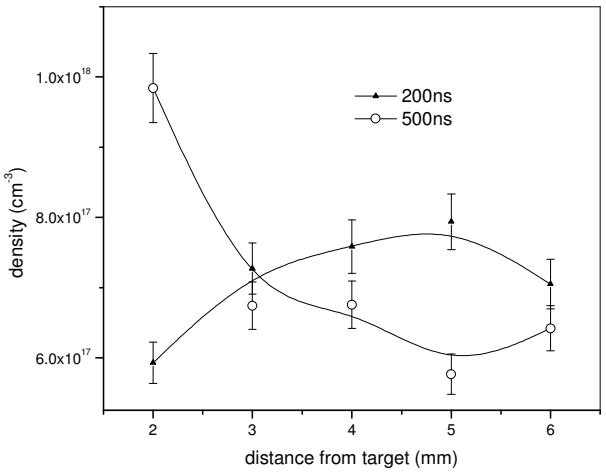

Fig. 2.29: Time resolved variation of spatial electron density. (source – LIP from aluminium metal)

From the density measurements made on the emissions collected in the far field (beyond 6mm distance from target surface) of the plasma, a density fall can be observed at later times (Fig 2.30-2.31). Another important feature observed is that the electron density profiles stretch over a longer distance as time increases, as a result of plasma expansion (Fig 2.30).

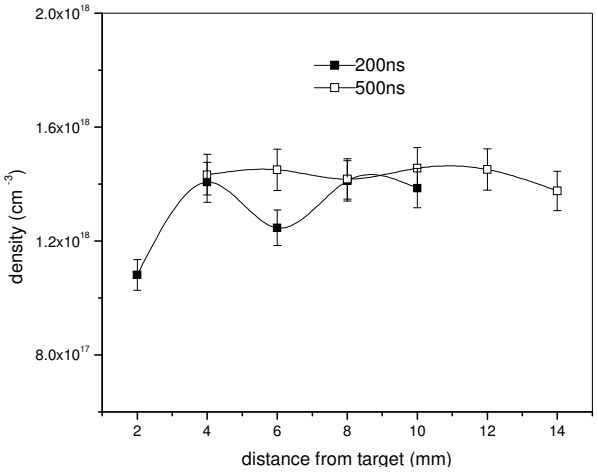

Fig. 2.30: Time resolved variation of spatial electron density extending up to far field of plasma. (source – LIP from aluminium oxide target)

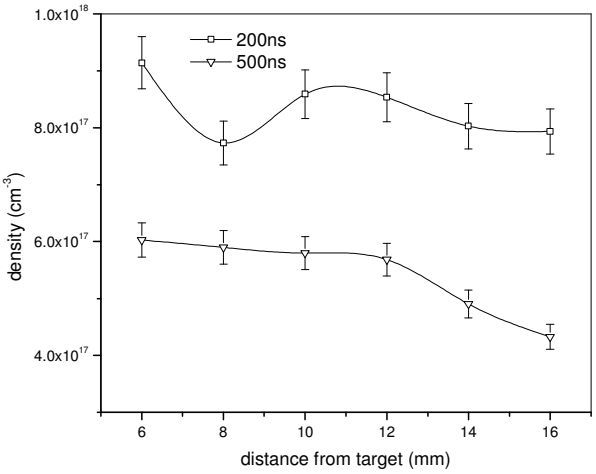

Fig. 2.31: Time resolved variation of spatial electron density. (source – far field region of LIP from aluminium metal)

As the plasma evolves between 200ns and 700ns, the range of plasma density variation is shortened in space, beyond 6mm (Fig.2.32). A flattening of the curve is also noticed at later times.

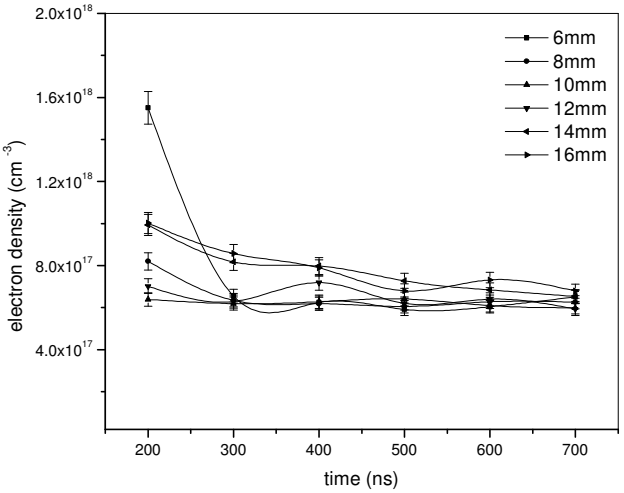

Fig. 2.32: Progressive flattening of electron density profile as time advances. Source – far field region of LIP from aluminium metal)

Considering that the plasma geometry is hemispheric [26], each axial position corresponds to plasma slices of different transverse extensions (hence volumes). As a consequence, the profile flatness suggests that the electron density is spatially homogeneous in the time range. These results do not contradict results obtained by other authors since as far as we know there is no report in the literature of time- and space-resolved electron density values for delays shorter than 1µm in the spatial range extending upto 16mm.

2.4.3. Evaluation of plasma temperature from line intensities of subsequent ionization stages: space and time evolution

The Boltzmann plot method is difficult to implement in this case as the lower energy levels of most of the experimentally convenient transitions are not well separated. This renders the line intensity ratios insensitive to temperature changes. Considerable improvement in the sensitivity is obtained if lines from successive ionization stages of the same element are compared with each other, because the effective difference is now enhanced by the ionization energy, which is larger than the thermal energy. In LTE, the ratio of such line intensities (I) follows the equation [27]:

$$\frac{I'}{I} = \frac{f'g'\lambda^3}{fg\lambda'^3}\left(4\pi^{3/2}a_0^3 n_e\right)^{-1}\left(\frac{kT_e}{E_H}\right)^{3/2}\exp\left(-\frac{E' + E_\infty - E}{kT_e}\right) \qquad (2.4)$$

Primed quantities in equation:2.4 refer to the line from the higher ionization stage, E_∞ is the ionization energy of the lower ionization stage, E_H is the ionization energy of hydrogen atom, a_0 is the Bohr radius, n_e is the free electron density, T_e is the electron temperature, g is the statistical weight and f is the oscillator strength.

The line intensities of Al I at 394.4nm ($3s^2.3p\ ^2P^0_{1/2} - 3s^2.4s\ ^2S_{1/2}$) and Al II at 390.1nm ($3s.3p\ ^1P^0_1 - 3p^2\ ^1D_2$) are compared in the spectroscopic evaluation procedure for temperature measurement. The presence of neutral lines characterizes the existence of non-ionized ablated matter in the plasma. The time integrated temperature falls with distance from the target (Fig: 2.33). Despite the expansive cooling, the decay rate falls, as the spatial point is more and more separated from the target. This may be due to the energy gained from three body recombinations [21].

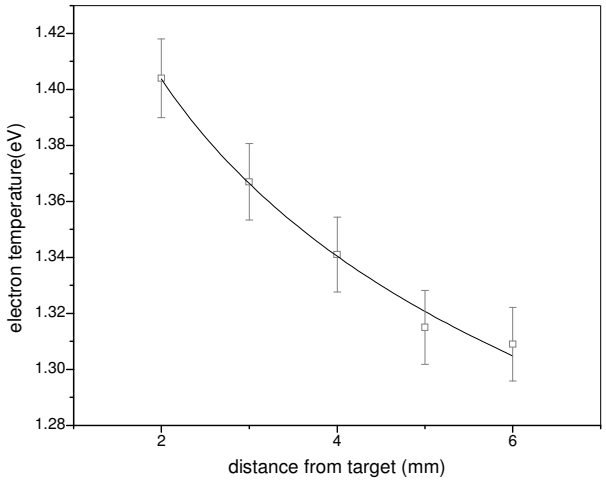

Fig. 2.33:Time integrated temperature values. Source – near field region of LIP from aluminium oxide.

This fact is also supported by the time resolved measurements (Fig: 2.34-2.35).

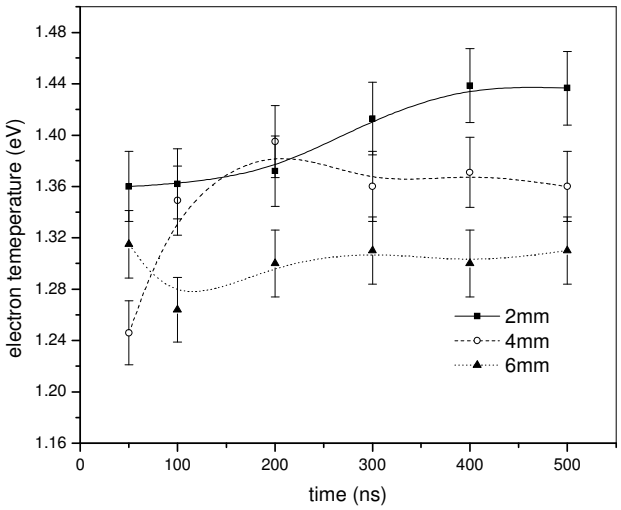

Fig. 2.34: Time resolved temperature plot of aluminium oxide LIP showing fall of temperature with distance from target.

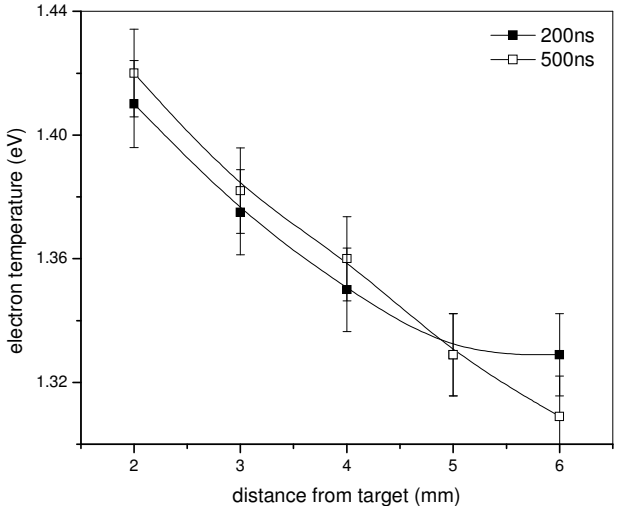

Fig. 2.35: Spatial variation of temperature in aluminium oxide LIP at different times

But for the plasma induced from the corresponding metallic target, a temperature drop is noticed at the target side. One of the reasons for the temperature drop noticed at the target side, at nearer spatial points is due to the thermal conduction from the plasma towards the solid target. The lowered temperature tries to build up even at nearer distances from the target as seen in the time resolved temperature values (Fig.2.36-2.37).

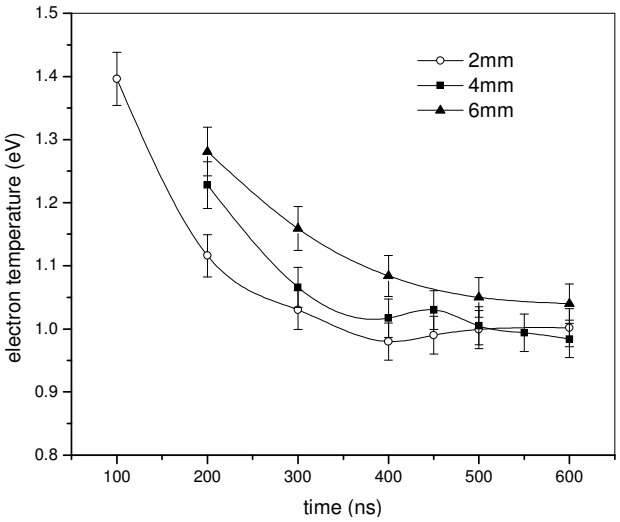

Fig. 2.36: Time resolved temperature plot of metallic aluminium LIP showing temperature drop at the target side.

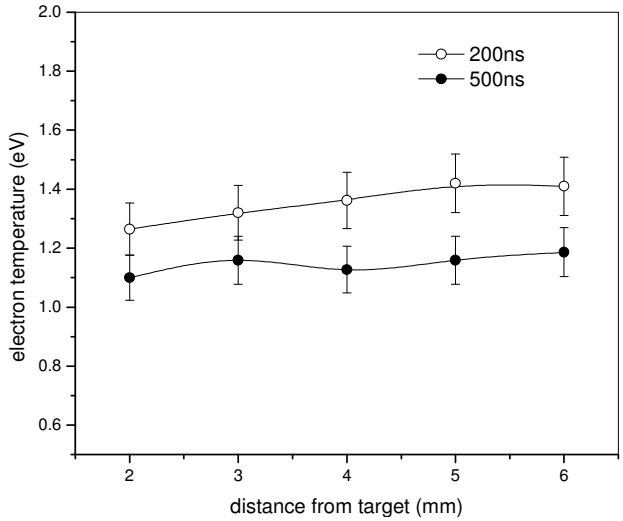

Fig. 2.37: Levelling of temperature in metallic aluminium LIP at intermediate spacial points (3-6mm).

At large spatial separations from the target, the time integrated temperature increases slightly. This is evident from the measurements on both types of aluminium targets (Figs. 2.38-2.39). This fact is also supported by the corresponding time resolved measurements (Figs. 2.40-2.43).

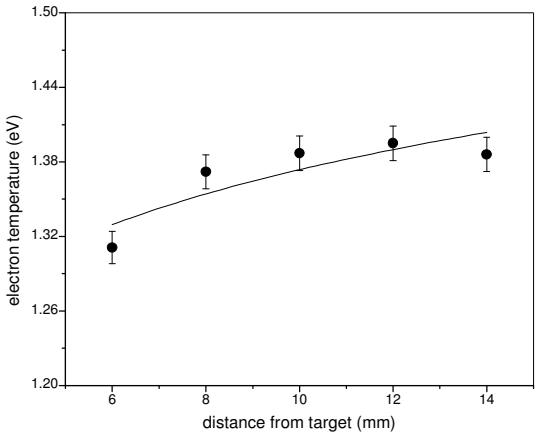

Fig. 2.38: Time integrated temperature values. Source – far field region of LIP from aluminium oxide.

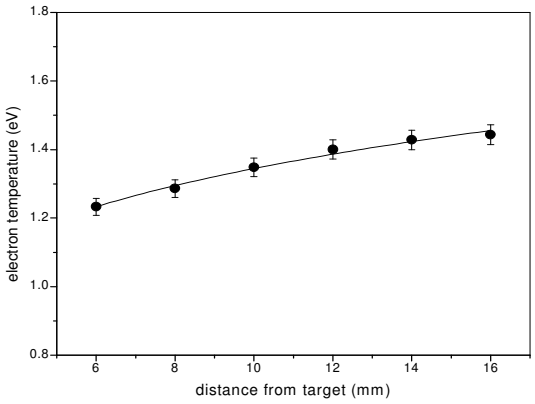

Fig. 2.39: Time integrated temperature values. Source – far field region of LIP from aluminium metal.

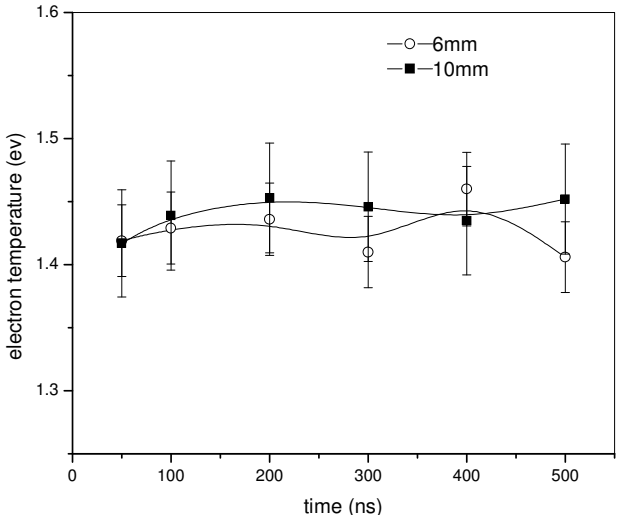

Fig. 2.40: Time resolved temperature. Source – far field region of aluminium oxide LIP

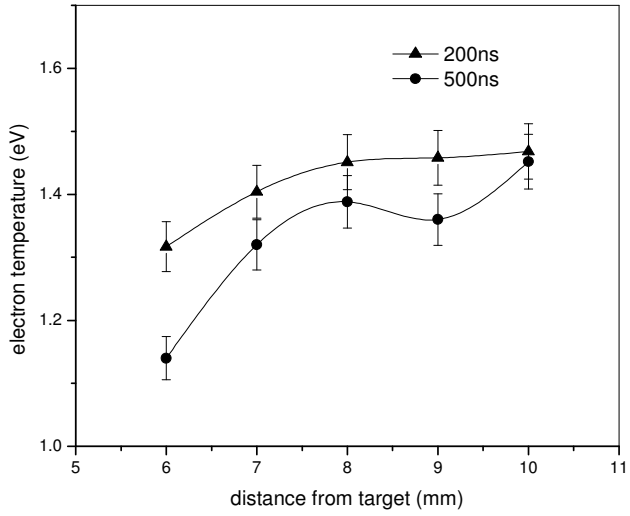

Fig. 2.41: Increase of temperature at large spatial separations. Source – far field region of aluminium oxide LIP.

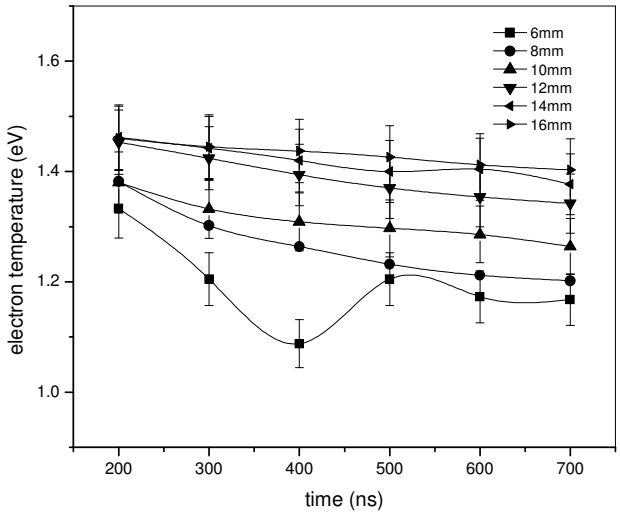

Fig. 2.42: Time resolved temperature. Source – far field region of metallic aluminium LIP.

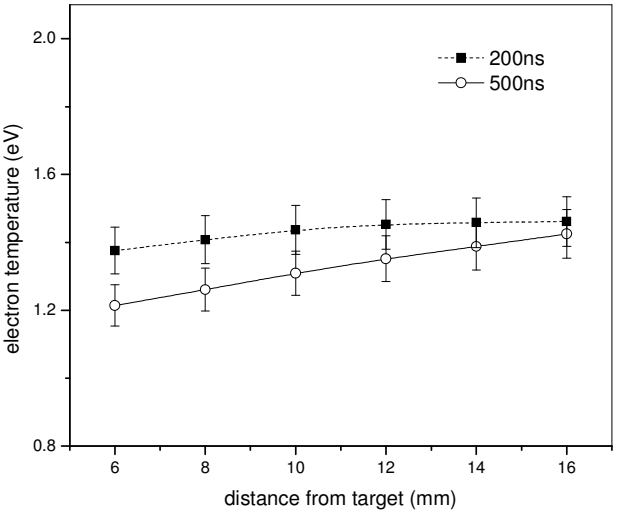

Fig. 2.43: Slight temperature increase at large spatial separations. Source – far field region of metallic aluminium LIP.

The temperature near the target shows steady decrease but at distances greater than 6mm, the temperature is found to increase. As the plume expands freely into vacuum, plume species move with different expansion velocities. The differential expansion becomes noticeable at farther spatial points and the separated species collide less frequently with one another. This reduces the rate of temperature equilibration and cooling. This fact is also responsible for the noted temperature increase.

The temperature drop at the plasma edge (on the right) is essentially due to radiative cooling, which is higher in this area as a consequence of the larger emitting surface. Heat conduction from the plasma to the ambient air also contributes to the plasma cooling at the front edge of the plasma. [28-32]. At early times, when the plasma is hot and dense, both plasma cooling effects are more significant than at later times, when thermal and radiative conduction have smoothed out the temperature gradients and lowered the plasma temperature values. The plasma temperature evolution at late times is largely determined by the cooling mechanisms (mainly radiation losses toward the ambient air) so that nearly the same ‘‘asymptotic state’’ is reached some time after the laser shot, whatever may be the initial conditions [31]. The leveling off of the temperature, amidst the expansive cooling at larger distances is mainly due to the energy gained from three-body recombination.

2.5. Tin oxide and tin

2.5.1. Emission profiles with pure and oxide targets

Two lines of *Sn* I, 452.5 nm with transition probability 2.6 x 10^7 s^{-1} ($5p \cdot 6s \ ^1P_1^0 - 5p^2 \ ^1S_0$ transition) and 615.5 nm with transition probability 11 x 10^6 s^{-1} corresponding to the transition, $6s \ ^1P_1^0 - 7p \ ^1D_2$, were selected for TOF measurements of neutral tin species. For investigating the flight of charged species in the plasma, two *Sn* II lines were selected. 559.6 nm line is arising out of the transition, $5s^2 \cdot 6d \ ^2D_{3/2} - 5s^2 \cdot 6p \ ^2P^0{}_{3/2}$, with transition probability 1.5 x 10^7 s^{-1} and 645.3nm $\left(5s^2 \cdot 6p \ ^2P^0{}_{3/2} - 5s^2 \cdot 6s \ ^2S_{1/2}\right)$ line has the transition probability 8 x $10^7 s^{-1}$. A typical plot for the flight of neutral species is presented in fig: 2.44.

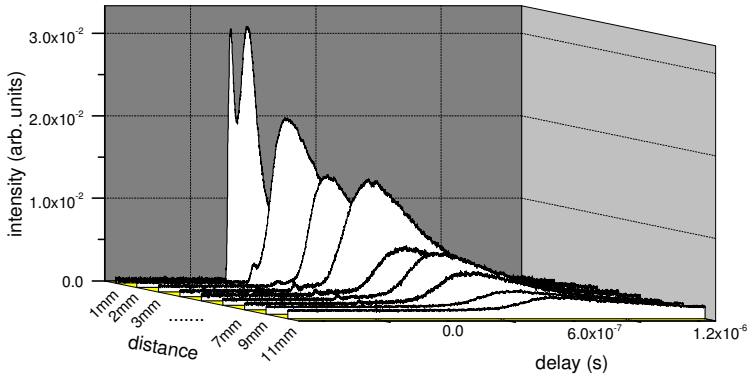

Fig. 2.44: Time of flight of neutral tin species (615.5nm) in tin oxide LIP

The expansion velocity of various plasma species is closely related to their charge states as well as their masses. The species with higher charge states move with high velocities compared to their counterparts with lower charge states [33, 34, 23].

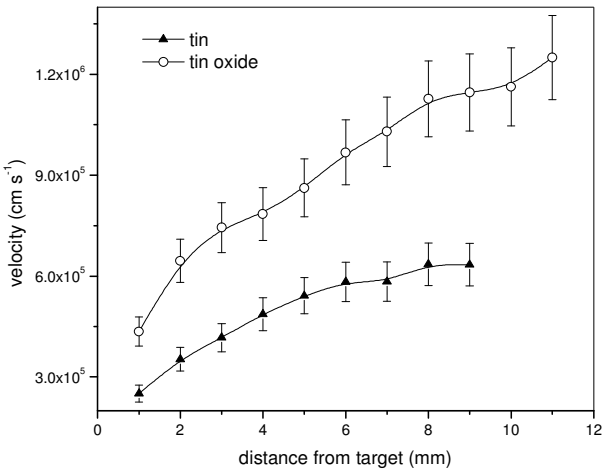

Fig. 2.45: Expansion (normal to target surface) of neutral species in tin and tin oxide targets.

During TOF separation, the observed velocity of flight of charged species is proportional to the square root of their charge to mass ratio. The observation that velocity of the neutral species are always lower than the singly ionized species is

made about LIP from pure metallic tin as well as tin oxide targets. But under the same conditions of vacuum and irradiance, neutrals and singly charged ions in the LIP from oxide targets gain comparatively higher flight velocities (Fig.2.45-2.46).

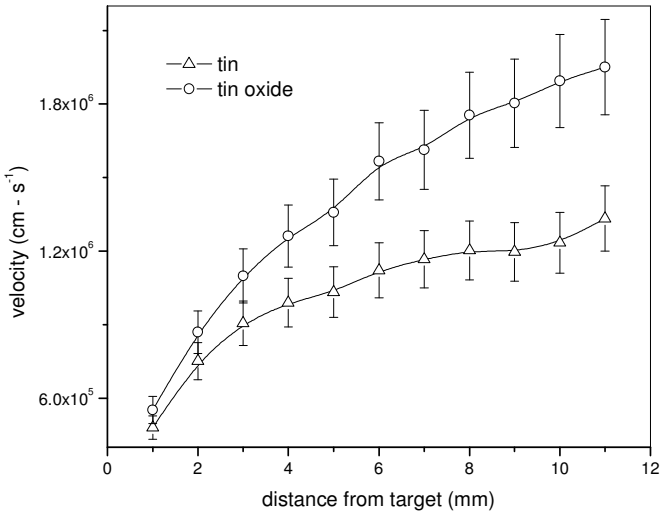

Fig. 2.46: Flight velocity of ionic species during forward expansion. Source – LIP from tin oxide.

2.5.2. Electron density evolution in space and time scales

Spectral measurements were made at sequential distances from the target surface upto 20mm. Spectral and line shape analyses were made at different distances from the target surface, on the Sn II line $\left(6p\ ^2P^0_{3/2} - 6d\ ^2D_{5/2}\right)$ at 556.2nm. The time integrated measurements are indicative of the average local conditions while the time resolved measurements are defining the conditions at a particular stage of the plasma's evolution. In tin plasma, density falls immediately up to 6mm, builds up slightly and thereafter the decrease is slow but (beyond 6mm) the oxide target develops a fluctuating density**,** about a mean value (Fig:2.47-2.48). This feature could be related to the change of the cooling mechanism from plasma propagation to recombination [35, 36].

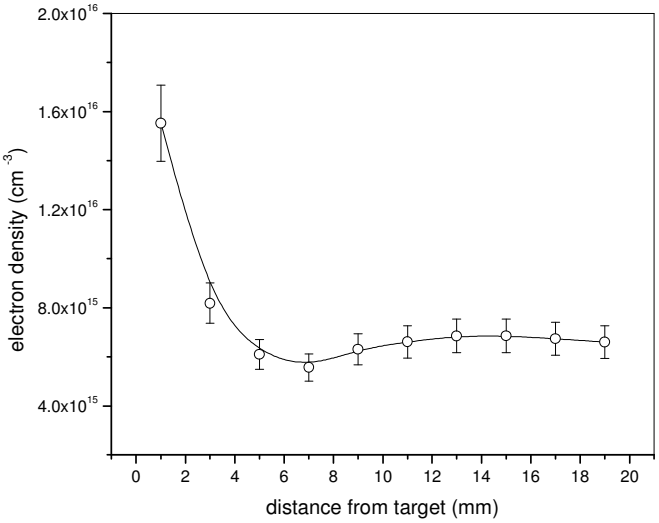

Fig. 2.47: Time integrated electron density in tin LIP.

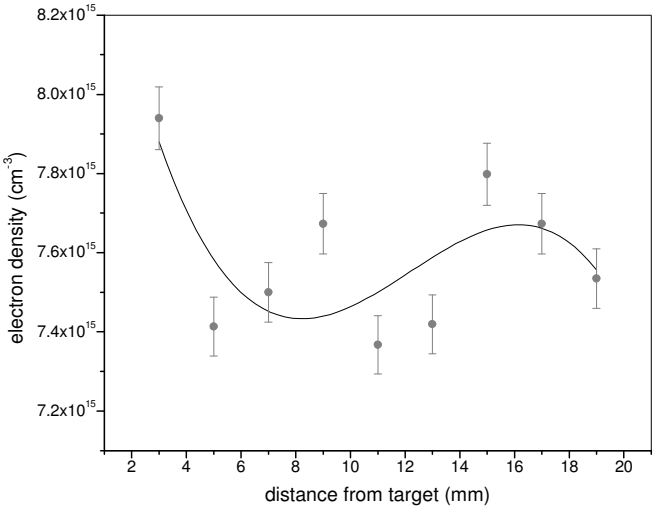

Fig. 2.48: Ttime integrated electron density in tin oxide LIP.

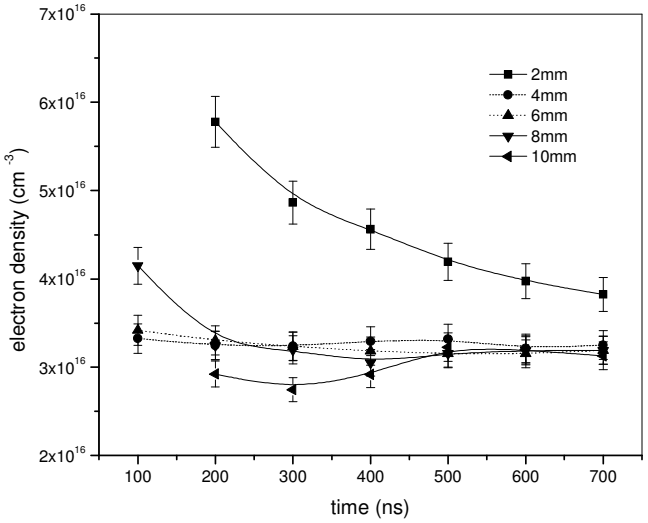

Fig. 2.49: Evolution of electron density during the initial expansion stage of tin LIP.

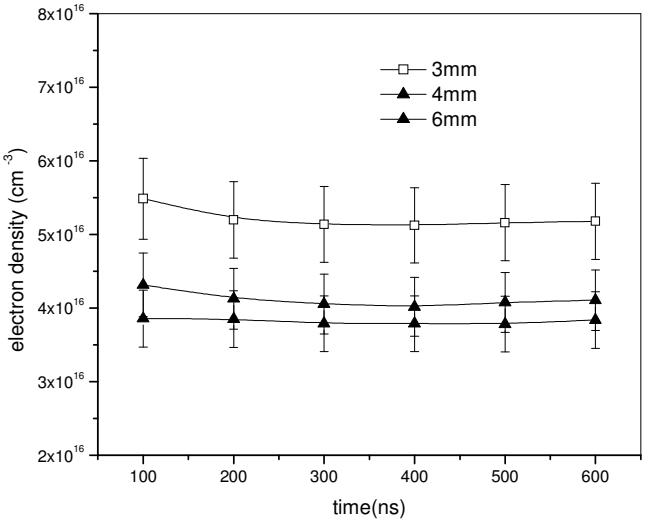

Fig. 2.50: Time evolution of electron density during the expansion of tin oxide LIP.

It is seen that the density attain its peak value close to the target surface within the first 100ns and then decrease due to the plume expansion. Initially the plasma expands isothermally during the laser pulse. After termination of the pulse, no more energy is pumped into the plasma. The thermal energy is converted into directed kinetic energy and the plasma cools through adiabatic expansion. After the plasma formation, the electron density over the LIP of both pure metallic and oxide targets of tin evolves nearly uniformly in time (between 200ns and 700ns) except at points closer to target surface, which shows relatively high values of density (Fig.2.49-2.50).

2.5.3. Calculation of plasma temperature along resolved space and time

It can be observed that somewhat larger data dispersion occurs in the evaluated T_e values, as compared to the electron density. This is due to the method (Boltzmann plot method) employed to extract the temperature, which requires the observation of seven spectral lines of various intensities, rather than only one for the determination of the electron density. Table 2.2 gives the spectral details used for calculating electron temperature.

wavelength (nm)	$A(s^{-1})$	g_m	species	E_m (eV)
556.2	13×10^7	6	Sn II	11.2
645.4	6.6×10^7	4	Sn II	8.97
684.4	6.1×10^7	2	Sn II	8.86

Table 2.2

A spectral response curve of the spectrograph+PMT, recorded in the region 400nm - 700nm has been used to calibrate the experimental line intensity values for the spectroscopic temperature measurement.

For tin targets, the temperature plot at 2mm is flat compared to 6mm where an increase of temperature is detected at later times (Figs.2.51-2.52).

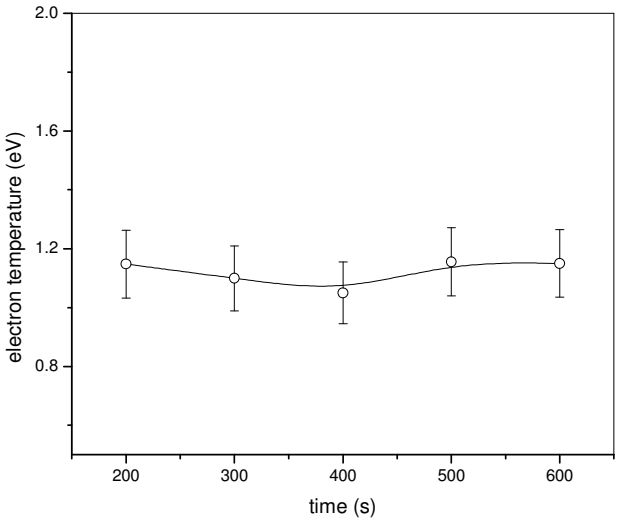

Fig. 2.51: Nearly flat time profile of electron temperature in tin LIP at 2mm.

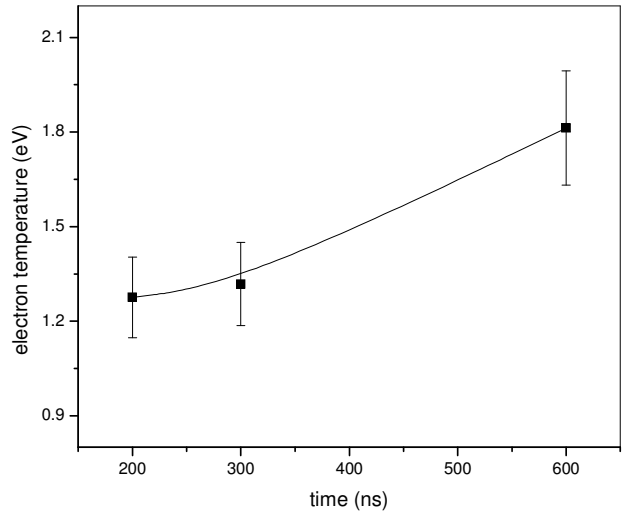

Fig. 2.52: Increase of electron temperature in tin LIP at 6mm as time evolves.

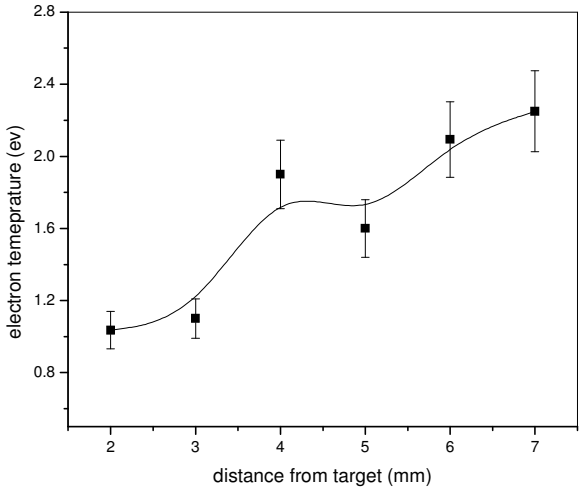

Fig. 2.53: Rise in electron temperature detected at farther spatial points of tin LIP during 500ns.

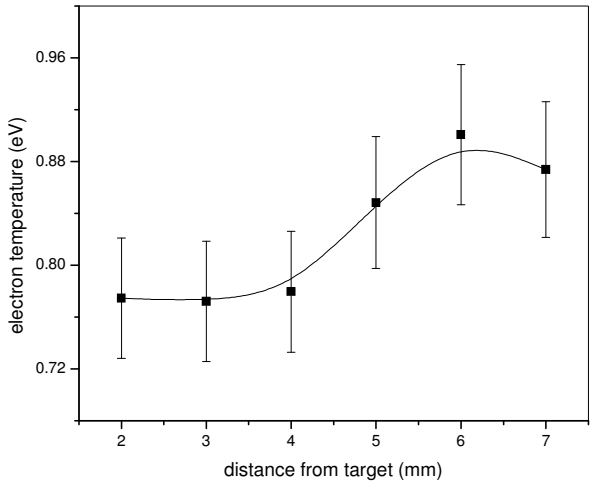

Fig. 2.54: Electron temperature increase at farther spatial points of tin oxide LIP at 500ns.

Except at spatial points closer to the target, a gradual rise in temperature is detected in LIP with both kinds of samples as targets (Figs.2.53-2.54)**.** This may be due to the absorption of laser energy by means of electrons via, the inverse bremsstrahlung absorption process and more details of this observation are presented at the end of section 2.3.3.

2.6. Summary

To conclude, LIP emissions from some metal oxide targets are studied with corresponding metal targets of pure quality as reference. Line emissions from atomic and ionic species are employed for the characterization. The studies provide improved insight, throwing more light into LIP dynamics.

2.7. References

[1] Anna Rita Casavola, Gianpiero Colonna, Alessandro De Giacomo, Olga De Pascale, and Mario Capitelli, Applied Optics Vol 42 No.30 (2003)

[2] Z. Szymanski, J Phys D: Appl Phys. 30 3153 (1997)

[3] Giacomo De, Shakhatov V A, Pascale O De., Spectrochim Acta Part B 56 753 (2001)

[4] Ludvik Martinu, J Vac Sci Technol A 18 (6) 2619 (2000)

[5] S. S. Harilal, Applied Surface Science 172 103 (2001)

[6] J. Hermann, J Appl Phys. 83 (2) 691 (1998)

[7] J. Hermann, J Appl Phys. 73 (3) 1091 (1993)

[8] M Capitelli, Spectrochimica Acta Part B 59 271 (2004)

[9] Colonna G, Casavolla A, Capitelli M., Spectrochim Acta B 56 567 (2001)

[10] J. Hermann, A. L. Thomann, C. Boulmer-Leborgne, B. Dubreuil, M. L. De Giorgi, A. Perrone, A. Luches, and I. N. Mihailescu, J. Appl. Phys. 77 (7) 2928 (1995)

[11] Dann V. J., Manoj V Mathew, V P N Nampoori et al, Proceedings of Fifth National Laser Symposium, (Vellore Institute of Technology, Vellore, India, December 7-10, 2005)

[12] Hermann J., Boulmer-Leborgne C, Hong D., J Appl Phys., 83(2) 691 (1998)

[13] Restrepo E., Devia A., J Vac. Sc. Tech., A 22 (2) 377 (2004)

[14] Singh R. K., Holland O W, Narayan J., J Appl Phys 68 (1) 233 (1990)

[15] Giacomo A De., Spectrochim Acta PART B, 58 71 (2003)

[16] A. De Giacomo, V. A. Shakhatov, G. S. Senesi, S. Orlando, Spectrochim Acta PART B 56 1459 (2001)

[17] Leon J. Radziemski, Thomas R. Loree, David A. Cremers, and Nelson M. Hoffman, Anal. Chem. 55 1246 (1983)

[18] Boumans P W J M, Theory of Spectrochemical Exitation (London: Hilger and Watts, 1966) ch 6, p 149

[19] A. Perea, J. A. Chaos, J. Gonzalo and C. N. Afonso, Appl. Phys. Lett. 78 7 (2001)

[20] Harilal S S, O'Shay Beau, Tillack Mark S., J. Appl Phys 98 13306 (2005)

[21] Bekefi G., Principles of laser plasmas, (New York : Wiley, 1976)

[22] S. Amoruso, A. Amodeo, V. Berardi, R. Bruzzese, N. Spinelli, R. Velotta, Appl. Surf. Sci. 96 175 (1996)

[23] Harilal S S, Bindhu C V, Tillack M S, Najmabadi F and Gaeris A C, J. Appl. Phys. 93 2380 (2003)

[24] V. Margetic, A. Pakulev, A. Stockhaus, B. Bolshov, K. Niemax, R. Hergenroder, Spectrochim. Acta Part B 55 1771 (2000)

[25] http://www.nist.gov

[26] O. Barthelemy, J. Margot, M. Chaker, IEEE Trans. Plasma Sci. 33 476 (2005)

[27] Hans R. Griem, Plasma Spectroscopy, (Mc Graw-Hill Inc, United States of America, 1964)

[28] F. Vidal, T.W. Johnston, S. Laville, O. Barthelemy, M. Chaker, B. Le Drogoff, J. Margot, M. Sabsabi, Phys. Rev. Lett. 86 (12) 2573 (2001)

[29] F. Vidal, S. Laville, T.W. Johnston, O. Barthelemy, M. Chaker, B. Le Drogoff, J. Margot, M. Sabsabi, Spectrochim. Acta, Part B 56 (6) 973 (2001)

[30] S. Laville, F. Vidal, T.W. Johnston, O. Barthelemy, M. Chaker, B. Le Drogoff, J. Margot, M. Sabsabi, Phys. Rev. E 66 (6) 066415 (2002)

[31] S. Laville, F. Vidal, T.W. Johnston, M. Chaker, B. Le Drogoff, O. Barthe´lemy, J. Margot, M. Sabsabi, Phys. Plasmas 11 (5) 2182 (2004)

[32] J.P. Christiansen, D.E.T.F. Ashby, K.V. Roberts, Comput. Phys. Comm. 7 271 (1974)

[33] Torrisi L and margarine D, Plasma Sources Sci. Technol., 15 635 (2006)

[34] Harilal S. S., Issac R C, Bindhu C V, Nampoori V P N and Vallabhan C P G, J Appl. Phys. 81 3637 (1997)

[35] M. Sabsabi, P. Cielo, Appl. Spectrosc. 49 499 (1995)

[36] L. St-Onge, M. Sabsabi, P. Cielo, J. Anal. At. Spectrom. 12 997 (1997)